Electro-Catalytic Properties of (100), (110) and (111) Oriented NiO Thin Films Towards the Oxygen Evolution Reaction

Raphaël Poulain,[1-2] Andreas Klein[2] and Joris Proost[1,*]

[1] *Université catholique de Louvain, Division of Materials and Process Engineering, Louvain-la-Neuve, Belgium*

[2] *Technische Universität Darmstadt, Institut für Materialwissenschaft, Darmstadt, Germany*

Abstract

Oriented NiO films (111, 100 and 110), reactively DC-sputtered on oriented platinum films on top of MgO substrates, were studied electrochemically on a rotating disk electrode for their performance towards the oxygen evolution reaction (OER). From the results, two electrochemical domains can be defined. At low overpotential (<1.55 V vs RHE), electrochemical performances are rather similar for all orientations. At higher overpotential (>1.55 V), the ranking is NiO 110 > NiO 111 > NiO 100. The observed differences were attributed to the fact that NiO 111 and NiO 100 produce an hydroxide phase with the same electro-catalytic properties, but the NiO 100 sample is covered less by the hydroxide and so produces less active sites. Moreover, NiO 110 forms the more stable and catalytically most active hydroxide phase. We attribute the observed differences to the formation of the β-NiOOH phase on the NiO 110 orientation, being more active than γ-NiOOH which is supposedly produced during the OER on the NiO 111 surface and, to a lesser extent, on NiO 100 surface orientation.

* Corresponding author : Phone +32-10-47.93.42 ; e-mail joris.proost@uclouvain.be

Introduction

In the frame of developing clean energy sources, hydrogen is viewed as a promising energy vector. The production of hydrogen is most often realized through the water splitting reaction in electrolysers or integrated systems such as photo-electrochemical devices. The hydrogen evolution reaction (HER) itself is relatively efficient, so that it is rather the oxygen evolution reaction (OER) that provides bottleneck issues and hinders greatly the performance of such systems. Indeed, OER involves four electrical charges where HER only requires two, decreasing greatly the kinetics of the reaction. Among all the parameters that can be tuned to optimize the reaction, the material used as electrode can have a great influence on the OER mechanism and so on the performance of the overall system.[1,2] The overall objective is to produce stable materials offering high current densities (> 0,5 A/cm²) at low overpotentials (< 0,3V).

Nickel hydroxide based electrodes appear to fulfil most of the requirements for being an ideal catalyst for the OER. A Tafel slope in the 40 mV/dec range has been achieved in alkaline media, especially when a little amount of iron is incorporated [3,4] Moreover, the material is electrochemically stable and lowly toxic. Nickel hydroxide forms layers maintained by a weak OH-OH bonding, in which Ni is found in octahedral positions.[5] Two hydroxide phases have been determined, the α and β phases. The α-phase is a pseudo-polymorph form of the β-phase where water and ions like K^+, OH^-, SO_4^{2-} and CO_3^{2-} intercalate between the hydroxide layers. The intercalated species act as an amorphous glue[6] and render the hydroxide layers free to displacement. As a result, the α-phase has a more elongated c-lattice which can reach up to 8 Å (a = b = 3,08 Å) whereas the c-lattice only measures 4,605 Å for the β phase[6]. Experimental results suggest that α-$Ni(OH)_2$ is not stable and tends to evolve into the β-phase when dehydration occurs, for instance during ageing or when the hydroxide is placed in vacuum[7]. During oxidation, Nickel hydroxide turns into Nickel oxy-hydroxide (NiOOH), the α and β hydroxide phases evolving into the γ and β oxy-hydroxide phase, respectively. The Bode diagram for the four phases is represented in Fig. 1. Note that the γ oxy-hydroxide phase is characterized by a higher Ni

oxidation state (3.5-3.67) than the β-oxy-hydroxide (2.7-3.0), and tends to transform to β oxy-hydroxide when aged.[8]

Bell *et al.*[9] reported that the electro-catalytic activity of nickel oxy-hydroxide was increased either by the incorporation of Fe in the γ-NiOOH phase, or by the phase transformation to β NiOOH when aged. However, Boettcher *et al.*[10] claimed that phase transformation is not the main mechanism explaining the increase of γ-NiOOH activity towards OER, but rather the gradual incorporation of Fe over time which stabilizes and crystallizes the γ oxy-hydroxide to the β phase. Advanced experimental and theoretical studies indicate that iron would substitute nickel in its octahedral position, shortening the Fe-O bond compared to γ-Fe-OOH and hence offering optimal catalytic site for the OER.[11] In any case, most studies agree that Fe is always present in its +III oxidation state while Ni would increase from +II to +III when a phase transformation from hydroxide to oxy-hydroxide occurs.[9]

Meanwhile, debate is still pending whether β-NiOOH or γ-NiOOH is the electrocatalytically more active phase for the OER[5]. This is partly related to a possible interference from the catalyst preparation method.[4] Most experiments on oxy-hydroxides consist in first electrodepositing $Ni(OH)_2$ on a metallic substrate (typically Au, Pd or Ni), which in fact are not stabilizing NiOOH in its β form. Instead, the electrodeposited $Ni(OH)_2$ layers always offer intercalation paths for external compounds, rendering the hydroxide turbostratic.[6] As a result, most experimental studies are carried out on γ-NiOOH and cycling for several hours needs to be realized in order to obtain β-NiOOH[7]. During this cycling step, iron can intercalate modifying both the oxy-hydroxide structure and composition or, in the absence of iron, the presumably obtained β turns into a γ oxy-hydroxide under over-charging conditions[4]. Theoretically, Li and Selloni[12] predicted by numerical simulation an overpotential of 0.26 V and 0.48 V for the OER on, respectively β- and γ- $Ni_xFe_{(1-x)}OOH$, so that it can be reasonably assumed that it is the β-phase which is the more active one, at least in the presence of Fe.

Among all the types of substrates on which nickel hydroxide can be grown, NiO has not been explored much in electrochemical water splitting devices, although it is a material of choice for many

applications. Indeed, NiO can be used as a protective layer for the anodic part of p-n buried junctions in integrated water splitting systems[13], and is being considered as a hole collecting layer in both Dye Sensitized Solar Cells and organic electronic devices.[14-18] NiO also gained recent attention in pseudo-capacitance applications, where energy is stored by Faradaic redox reactions in the Helmholtz double-layer[19-20]. Some studies even consider to introduce NiO in silicon based solar cells[21]. However, only a few reports consider the use of NiO as an OER catalyst. Miller *et al.*[22] have been the first to suggest that the OER activity can be increased with NiO sputtered films, at least when they presented a high degree of crystallinity and in the presence of a large excess of oxygen in the film. This excess of oxygen would lead to a pronounced formation of Ni^{+3} in the film, hence increasing the catalytic activity towards OER while still conserving the NiO structure[23]. The study of Miller also suggested a dependence of the OER activity on the crystal orientation of sputtered NiO, but completely ignored the importance of nickel hydroxide formation. The relevance of considering the crystal orientation has been demonstrated already in the case of IrO_2 and RuO_2, where the thermodynamically unstable 100 orientation was shown to more active towards OER than the 110 orientation.[24]

Structurally, NiO is a stacked rocksalt-like structure with a lattice constant of 4.17 Å. Three possible surface orientations can be obtained: 100, 110 and 111, as shown in Table 1. The 100 and 110 orientations are non-polar, meaning the electric charge with the underlying plane is neutral, while the 111 orientation is polar because of the formation of a dipole perpendicularly to the surface[25]. The lowest surface energy is obtained for the NiO 100 orientation at 1.15 J/m^2, which is more than half the value for the 110 surface[26]. The 111 orientation is the most densely populated surface and has a theoretically infinite surface energy[26]. As a result, NiO 111 surfaces usually undergo structural surface faceting, either by 100 pyramidal faceting[27-29] or by p(2 x 2) octopolar reconstruction[30-33], or can be subject to chemical bonding with hydroxide[34-35]. Theoretical work on the adsorption energies for H_2O and OH^- on pure Ni surfaces indicate a decrease in the order Ni(110) > Ni(100) > Ni(111), and for O and H atoms the adsorption energies decrease in the order Ni(100) > Ni(111) > Ni(110).[36] Also the Ni hydroxide properties can be orientation-dependent, as shown by Tench and Ogden on oriented Ni

crystals, Ni(111) forming the more stable hydroxide in acidic media.[37] To the best of our knowledge, no experimental study has been carried out up to now on the NiO surface dependence of the OER electrochemical activity. The aim of this study is therefore to combine electrochemical results obtained on oriented NiO films with a number of structural characterizations. This will not only provide guidelines for the tailoring of NiO based electrodes for OER, but will also highlight the fact that the NiO electrochemical properties are closely related to the Ni hydroxide being formed on its surface during anodic polarization.

Experimental section

Sample preparation

Oriented samples were prepared from (111), (110) and (100) oriented MgO substrates on which oriented Pt films were grown. NiO was then DC sputtered reactively at 500°C in an unbalanced magnetron cathode configuration from a pure Ni target. According to literature reports, the NiO 100 and NiO 111 orientation are being favoured at low and high oxygen concentration, respectively [38-39]. Hence, films were deposited with 10 % of oxygen to a thickness of about 100 nm for the 100 orientation, and 20 % of oxygen for the 111 and 110 orientations which were about 150 nm thick. All other sputtering conditions were the same for the three oriented samples, and summarized in Table 3. Note that the expected $Ni(OH)_2$ thickness is in the nm-range, so that, contrary to the case of metallic Ni thin films, there should be no "mass" limitation whatsoever with respect to any possible Ni oxyde-hydroxyde transformation during OER. The use of platinum as an underlayer is motivated by the fact that a Pt/NiO junction should create an ohmic contact. Indeed, the work function of p-type NiO is typically less than 5.1 eV, while metallic Pt has a work function strictly above 5.1 eV. As a result, a charge accumulation layer should be created in the NiO at the Pt/NiO interface.

Electrochemical experiments

All experiments have been realized at room temperature in ultra-pure 1.0 M KOH electrolyte (Semi-conductor grade, 99,99% trace metals, Sigma-Aldrich). Samples were fixed at the tip of a rotating disk (2000 rpm) and measured against a Ag/AgCl reference electrode, the latter having a potential of 0.95 V vs RHE. Electrochemical measurements were realized with a Metrohm Autolab PGSTAT302N potentiostat, equipped with FRA 32M impedance and SCAN250 modules. A schematic description of the main experimental steps is given in Figure 2. They consisted in a CV activation at 100 mV/s for 10 scans, followed by a chrono-amperometric measurement for 10 min at 1.65 V vs RHE (0.7 vs Ag/AgCl) to ensure the electrode is in its equilibrium state. Then a slow CV is realized twice at 10 mV/s, followed by a quasi-static experiment. The latter consisted in fixing the working electrode potential for 90 sec while current is being measured. Between each potential plateau, the potentiostat is switched off, meaning no current is circulating but any oxygen bubbles stuck to the sample surface are still being flushed away. The current value at the end of the span time is then taken to construct I-V curves. Finally, Electrochemical Impedance Spectra (EIS) are carried out from 1 MHz to 1 Hz at different potentials, while the series resistance is determined for iR correction of the I-V curves. Contrary to NiO 111 and NiO 110, the NiO 100 sample produced three semi-circles during EIS, so that the NiO 100 I-V curve was corrected by $R_{tot} = R_{contact} + R_{semi\text{-}circle\ 1} + R_{semi\text{-}circle\ 2}$ for which semi-circle 1 and semi-circle 2 are the semi-circles visible at high frequencies (>100 kHz). The thus obtained series resistance values are given in Table 3 for all surface orientations. The equivalent capacitance C_{eq} from the constant phase element representing the Helmholtz layer was determined by the following equation, as proposed by Musiani *et al.*[40] :

$$C_{eq} = Q^{\frac{1}{\alpha}} * \left(\frac{R_{el} * R_{cpe}}{R_{el} + R_{cpe}}\right)^{\frac{1-\alpha}{\alpha}} \quad (1)$$

Structural characterization

Before the electrochemical experiments, X-ray θ/2θ scans were realized with a Bruker D8 Advance diffractometer with a Cu X-Ray source. Calculation of relative peak heights was done by simple area integration corrected by their relative intensity (PDF-2-card-4835). XRD patterns were also realised after electrochemical cycling. These were performed with a Seifert PTS 3003 diffractometer using a Cu anode and an X-ray mirror on the primary side, operated at 40mA and 40 kV. On the secondary side, a long soller slit and a graphite monochromator was used to separate the Cu K-α line. AFM measurements have been realized before electrochemical experiments as well. Surface mapping was done with a Bruker Icon Dimension in tapping mode.

Finally, XPS measurement were performed ex-situ after the electrochemical measurements, in order to help identifying the adsorbed species at the surface and hence to address the differences in the observed electrochemical activity of the differently oriented samples. XPS measurements were realized with a system based on K-Al lamp emitting a monochromatic X-ray wavelength of 1486 eV. O1s and Ni2p(3/2) peaks were scanned in order to obtain quantitative data. XPS fitting was realized with CASA XPS software and were focused on the O1s peak. Fitting was based with three Gaussian-Lorentzians (GL – 15), with O-C, O-H and O-Ni constrained to be in the range 532.7-532.9 eV, 530.9-531.9 eV and 529-530 eV, respectively. FWHM of the oxygen peak associated to carbon was fixed to be the same as the oxygen bonded to hydroxide. It should be noted that these XPS measurements did not allow to differentiate between the hydroxide phases, as the imposed vacuum conditions would lead to water removal and nickel hydroxide crystallization in its β phase[7].

Results

Structural characterization

The X-ray diffractograms in Figure 3 reveal in all cases oriented films along the c-axis, although the inclusion of non-desired orientations in NiO 110 and NiO 100 needs to be recognised. In the NiO 110 film a small fraction of NiO 100 can be seen, while in the NiO 100 we observe NiO 111. However, it remains marginal and it can be assumed that the electrochemical properties will be mainly related to the main orientation. When comparing the XRD-patterns before and after electrochemical cycling, it can be observed that the main orientation of the samples is preserved. However, it seems an additional phase appears on the 111 sample after OER, but this could not be identified to any hydroxide phase from our database. In any case, due to the low hydroxide thickness measured by XPS (1-2 nm), it should not be possible to measure any hydroxide phase by XRD. On the 100 sample, it cannot be excluded that the observed shoulder, both before and after OER, is associated with non-oxidised metallic Ni being incorporated in the NiO thin film as a result of the relatively low oxygen concentration during reactive sputtering (10% compared to 20% for the two other samples). Since the oxygen gas inlet is only cut once the sample is sufficiently cooled down (< 100°C), any metallic Ni remaining on the outer part of the film will probably be oxidized. Therefore, we can assume an oxygen gradient exists throughout the NiO 100 film, which could lead to a charge depletion layer between the bulk of the film and the electrolyte. On the other hand, the (110) and (111) films seem to be oxidized homogeneously along the film thickness.

Before electrochemical testing of the three studied samples, the AFM micrographs in Figure 4 show flat and cubic grains for the NiO 100 sample. This indicates that we have an excellent surface orientation, in agreement with other results from the literature.[41] The NiO 110 direction displays more elongated grains and adopts specific regular patterns, which also indicates that the film adopts an oriented structure. The NiO 111 film has the most surprising surface morphology. Indeed, the structure seems to develop two surface domains : one leading to an apparent (111) flat surface and the second leading to a rough surface but without any surface faceting. The exact mechanism leading to such

surface inhomogeneity is out of the scope of this work. Nonetheless, the fact that we have a relatively flat (111) surface without reconstruction correlates well with recent literature reports stating that pyramidal reconstruction into (100) faceting is only obtained at lower oxygen concentration during reactive sample preparation.[42] Before the electrochemical experiments, the flattest surface is obtained with the NiO 100 sample, and in comparison geometrical surfaces are only slightly higher for NiO 110 and 111 (2.2% and 4.7% respectively, cfr. Table 4). We can therefore reasonably assume that the influence of the geometrical surface can be neglected when interpreting the electrochemical experiments.

The XPS measurements in Figure 5, which have been realized after electrochemical cycling, reveal noticeable differences between each sample. The peak in the 856 eV range, associated with $Ni(OH)_2$ and accompanying at higher binding energy the Ni2p(3/2) peak, is the strongest for the NiO 110 sample, followed by NiO 111 and then by NiO 100. After deconvolution of the O1s peak, a higher hydroxide coverage on the NiO 110 over the NiO 111 and 100 surfaces can be determined. The estimated thickness of the hydroxide layer are 2.1, 1.7 and 1.4 nm for NiO 110, 111 and 100, respectively (cfr. Table 5). Thus, the lowest hydroxide coverage is produced on the NiO 100 film surface. Additional XPS was also performed to specifically address the potential issue of iron contamination. The result, shown in Figure 5.c, indicates the absence of any Fe on the surface, at least under the detection limit of the device (<1%) and according to the reference data taken from McIntyre.[43]

It should be noted that, since hydroxyl attachment occurs specifically on the Ni cationic site, the density of Ni-atoms on the various surface orientations needs in principle be taken into account as well when addressing differences in the extent of $Ni(OH)_2$ coverage. Therefore, we have included in the first row of Table 5 also the theoretical density of Ni cations per surface area for the different NiO surface orientations, based on the surface data already provided in Table 1. It can be observed that, while the

NiO 110 surface provides in theory the lowest number of cationic sites per unit surface area, it has nonetheless the highest measured hydroxide surface coverage. Similarly, the NiO 100 surface has the lowest measured hydroxide thickness, although its theoretical Ni atomic surface density is intermediate between NiO 110 and 111. This clearly indicates that the cationic Ni surface site density on the differently oriented NiO samples does not correlate with the measured hydroxide thickness.

Electrochemical measurements

Figure 6 (left) presents the I-V data obtained from both the slow CV sans (at 10 mV/s) and the quasi-static experiments. It can be seen that, while a small voltage offset is observed for the NiO 111 and 100 samples, they are superposing relatively well for the NiO 110 orientation. This is consistent with earlier reports that nanopellets with dominantly 110 exposed surfaces had extended stability over long cycling tests and fast discharge behaviour of intercalated ions with high columbic efficiency.[44] When plotting the I-V curves semi-logarithmically (Figure 6 right), two regimes of electro-catalytic activity are being highlighted. The first one, at low overpotential (1.45 – 1.55 vs RHE, I < 2 mA/cm²) is characterized by a high electro-catalytic activity (low Tafel slope), while the second regime at potentials above 1.55 vs RHE (I > 10 mA/cm²) develops lower electro-catalytic activity (high Tafel slope). It can hereby be assumed that any mass transport limitation is negligible at high over-potentials. Indeed, when applying the Levich equation (2) to our system

$$I_{LA} = 0.620 * n * F * D^{\frac{2}{3}} * v^{-\frac{1}{6}} * C_R * w^{\frac{1}{2}} \qquad (2)$$

n being the number of electrons exchanged, *F* the Faradic constant, *D* the diffusion coefficient of hydroxyl in water ($\cong 10^{-5}$ cm²/s), C_R its concentration in mol/cm³ and *w* the angular rotation speed (210 rad/sec at 2000 rpm), calculation gives an anodic limiting current I_{LA} of 900 mA/cm². This is far beyond

the current range in which the set-up is working (< 100 mA/cm²). Moreover, surface reduction because of oxygen bubbles being stuck to the rotating electrode surface can be ruled out as no big variation in current is observed, neither during the chrono-amperometry, nor during the quasi-static experiments. Therefore, from the observed differences in Tafel slope, it can be assumed that different electrochemical reaction paths are taken at low and high overpotential, respectively. It is noteworthy to report that Nadesan *et al*. [23] observed three Tafel slopes on their NiO, the first region being limited to currents below 5 mA/cm², then a region for which current is comprised between 5 and 100 mA/cm², and the last region for currents higher than 100 mA/cm².

In our own case, at low overpotentials, the Tafel slope can be considered to be similar for all surface orientations, as shown in Figure 7. It averages to a value of 48 $\pm$ 8 mV/dec during the QS measurements, statistically equal to the average value of 54 $\pm$ 8 mV/dec obtained at 10 mV/s. At high overpotentials, the NiO 110 clearly gives the lowest Tafel slope. When looking at the I-V curve in log scale of the NiO 100 and the 111 samples, they have very similar shapes, the NiO 111 sample just being shifted upwards by about 0.25 decades.

Secondly, we can take a look in Figure 8 at the fast CV scans at 100 mV/s with respect to the current wave typical of hydroxide/oxy-hydroxide phase transformation situated just before the OER. A clear difference can be observed between the three samples, which has further been quantified in Table 6. The backward columbic charge represents around 85-87% of the measured forward columbic charge for the NiO 111 and NiO 100, while it reaches up to 115% for the NiO 110 sample. Moreover, the transformation of the $Ni(OH)_2$ to the NiOOH phase occurs at lower potential for NiO 100 as compared to NiO 111 and 110, especially during the backward scan. Such a lower potential for the reduction peak is typically associated with the production of the turbostratic α-phase, while a higher reduction peak would be indicative of the more crystallized β-phase[45].

Thirdly, the results in Figure 9 from Electrochemical Impedance Spectroscopy (EIS) provide again noticeable differences between the three samples. We already pointed out before that an oxygen gradient can be assumed throughout the NiO 100 film, which also leads to a hole depleted layer between the bulk of the film and the electrolyte. As a result, a less conductive layer emerges between the bulk of the sample and the electrolyte, explaining the presence of an additional capacitive component in the EIS spectra. The latter can, in the high frequencies range (>100 kHz), then be fitted with a specific model including both a space-charge layer, surface states and a Helmholtz layer,[46] as represented in Table 7. Interestingly, from analysing the EIS spectra for the (100) sample, the capacitance value associated with the space charge layer can be considered to be purely capacitive and therefore not affected by the potential value, which supports the existence of a somewhat buried junction. On the other hand, the (110) and (111) films seem to be oxidized homogeneously along the film thickness, and might even include Ni^{3+} species which could bring additional charge affecting the NiO workfunction. As a result, EIS results on (110) and (111) samples show the typical semi-circle evidencing the presence of a Helmholtz double layer, for which the turnover frequency is less than 1 kHz and which can simply be fitted by a R+(CPE/R) model (cfr. Table 7). All extracted parameter values from fitting the EIS spectra to these respective equivalent circuits are shown in Table 8, while Figure 10 represents fitting results for the current density dependence of the equivalent capacitance of the Helmholtz double layer (C_{eq}, top), as well as the charge transfer resistance (R_{ct}, bottom).

Regarding the Helmholtz double layer, charge depletion at the electrode/electrolyte interface can be understood from the band energy diagram. Indeed, the equivalent work function of an electrolyte of pH 14 can be assumed to be around 3.7 eV,[46] while the NiO work function is expected to be more than 4 eV. Therefore, interfacing NiO with an electrolyte of pH 14 should lead to the creation of a hole depleted region of a few hundred meV. Moreover, the N-factor in Table 8 related to the CPE representing surface states in NiO 100 is comprised between 0.65 and 0.8 over the studied range of potentials, meaning the associated capacitance is rather inhomogeneous. On the contrary, EIS on NiO 111 and 110 samples are not marked by a possible hole depleted region in the NiO film, nor the

presence of surface states. This can be attributed to the fact that these two orientations, contrary to NiO 100, offer enough adsorbing sites fixing hydroxide from the electrolyte at the top surface. In other words, for NiO 100 additional charges need to be drawn to the surface to compensate the charge forming at the electrolyte interface.

With respect to the charge transfer resistance, Figure 10 (bottom) shows that it varies very similarly for the (111) and (100) samples over the studied range of current densities (0.1-40 mA/cm^2). This can be taken as indirect evidence that the hydroxyde phase being formed on these samples is identical in nature as well. However, their values are about 2 times lower than for the (110) orientation. As a result, this difference in contact resistance cannot explain why at high polarization the (110) sample has the lowest Tafel slope, and hence the best electrocatalytic performance, over the other oriented samples.

Discussion

NiO (100) vs. NiO (111)

The observed vertical upward translation in Fig. 6 between the log(I) vs. V curves of NiO 111 vs. NiO 100 is a direct result of the same Tafel slopes, and therefore indicative for the fact that the same catalytic activity is obtained for both surface orientations. In other words, the same hydroxide sites are active on both surfaces, but the amount of the hydroxide coverage should be higher on the NiO 111 sample than on the NiO 100 sample. Indeed, a translation in the Tafel plots can be interpreted by a higher pre-exponential factor for the 111 sample. Having a similar log plot shape and the same frontward/backward columbic charge ratio (cfr. Table 6), it can be assumed that the same active hydroxide phase is being formed on the surface. Moreover, since AFM measurement do not highlight a clear surface increase for the 111 sample over the 100 sample (only 4.7%, cfr. Table 4), the translation can be fully attributed to an increase of the hydroxide surface coverage on the 111 sample compared to the 100 sample. The observed translation in Fig. 6 represents an increase of about 77%

of the surface covered by the hydroxide. This increase is, at least qualitatively, in line with a number of other observations : the higher columbic charge in the NiOOH $\rightarrow$ $NiO(OH)_2$ region of the NiO 111 sample as compared to NiO 100 (x 3.5, cfr. Table 6), the XPS measurements which confirm a higher hydroxide thickness on the NiO 111 surface than on the NiO 100 (x 1.4, cfr. Table 5) and the fact that the Helmholtz double layer is higher on NiO 111 than on NiO 100 (x 1.5, cfr. Fig. 9). The fact that NiO 111 develops a higher hydroxide coverage than NiO 100 is also consistent with the work of Cappus *et al.*[47] Their work suggests that hydroxyl groups do not bond to regular sites on a NiO 100 surface but rather to defective ones, while a full hydroxyl coverage is obtained with a NiO 111 surface. Moreover, Schulze *et al*.[48] reported that, as opposed to NiO 111, water does not dissociate on NiO 100, neither on a smooth surface nor on a defective surface, and that produced oxygen tends to heal the defective sites on a NiO 100 surface. During electrochemical experiments, the hydroxide on the NiO 100 surface is therefore probably formed on defective sites only (e.g. grain boundaries), instead of on regular sites for NiO 111.

NiO (110) vs. NiO (111)

From its lower Tafel slope in Fig. 6, the NiO 110 orientation shows higher catalytic activity for the OER than NiO 111, particularly at high over-potential (> 1.55 V vs RHE). It can therefore be assumed that different hydroxides are formed for each orientation. In this respect, it was shown in Table 6 that hydroxide oxidation to oxy-hydroxides (NiOOH) produces an equivalent columbic charge that is about 1.5 times higher for NiO 111 as compared to NiO 110. At the same time, XPS measurements in Table 5 indicated that the hydroxide layer is slightly thinner (factor 0.9) on NiO 111 than on NiO 110. The equivalent capacitance of the Helmholtz double layer has a similar value for both samples with a CPE N-factor above 0.9. This indicates that the hydroxide layer is homogenous on both samples with an equivalent hydroxide surface coverage in contact with the electrolyte. As demonstrated in Table 9, the NiO 110 surface can therefore be assumed to produce a thicker hydroxide layer with a lower Ni

oxidation state typical of β-NiOOH. The latter table shows the number of exchanged electrons per cationic site during the pre-OER hydroxide/oxy-hydroxide forward (FW) oxidation wave, based on the values for the theoretical Ni-atomic density and the number of electrons per unit surface that can be determined from the specific charge values in Table 6. Dividing these values by the cationic density of $Ni(OH)_2 \cong 0.026$ Ni/Å^3,[6] we can then also come up with an "electrochemical" estimation of the Ni hydroxyde thicknesses. For the latter, two cases need to be considered, depending on whether pre-OER oxidation produces the oxy-hydroxyde β or γ phase. Indeed, according to the Bode plot in Figure 1, the corresponding increase in oxidation number will be +1 (2→3) or +1.67 (2→3.67) for the β or γ phase, respectively.[11] Since the estimated electrochemical hydroxyde thickness cannot be higher than the one measured experimentally by XPS, we can then reasonably assume that the number of electrons exchanged for the hydroxide on the (111) surface is 1.67 (β→β phase), while the one for the (110) sample would need to be 1 (α→γ phase). Moreover, it has been shown that β-$Ni(OH)_2$ has a much better capacity retention over the alpha phase, meaning most of the electrochemical energy during the oxidation to their respective oxy-hydroxides is returned upon reduction, even reaching columbic efficiency superior to 100%[21]. This is consistent with our own observation in Table 6 that the columbic charge for the NiO 110 sample is higher for the backward scan than for the forward one. In conclusion, it is very reasonable to assume that the NiO 111 surface would produce an hydroxide mainly made of α-$Ni(OH)_2$, while the NiO 110 would be likely producing the β-$Ni(OH)_2$ phase, which then also remains more stable upto high over-potentials.

Tafel slope values

The above discussion on the Tafel slope values obtained for the various surfaces both at low and high polarization provided a first insightful but still qualitative figure of merit for linking the electro-catalytic behaviour of the differently oriented samples with the underlying mechanistic details of (oxy-)hydroxyde formation, in terms of the degree of hydroxyde coverage and the nature of (oxy-)hydroxide

phase formation. To make the discussion more quantitative, it is still an open question to what extent the experimental Tafel slopes can be related to the nature of the rate determining step in the OER. In this respect, the necessary rate equations and theoretical Tafel slopes have been derived in ref. 49 for a number of aqueous electrocatalytic reactions involving gaseous H_2 or O_2 (including HER, HOR, and ORR and OER). The particular relevance of this reference for our work lies in the fact that it explicitly demonstrates that Tafel slopes that are generally used to evaluate underlying rate determining steps often rely on over-simplified rate equations that assume extreme surface coverage of the adsorbed species ($\theta \cong 0$ or 1), while in theory, these slopes are coverage-dependent. Specifically in the case of OER in alkaline media, which is the reaction of interest for our work, the following reaction mechanism can be considered (assuming a single-site mechanism, M denoting an empty site on the surface) :[49]

$$M + OH^- \leftrightarrow MOH + e^- \quad (3)$$

$$MOH + OH^- \leftrightarrow MO + H_2O + e^- \quad (4)$$

$$MO + OH^- \leftrightarrow MOOH + e^- \quad (5)$$

$$MOOH + OH^- \leftrightarrow MOO^- + H_2O \quad (6)$$

$$MOO^- \leftrightarrow M + O_2 + e^- \quad (7)$$

Each of these steps can potentially become rate-determining, and the rate equations for each step were shown in ref. 49 to be highly dependent on the relevant coverage expressions θ_i for each step (*i* being either the empty site, MOH, MO, MOOH or MOO^- respectively). A lower value of the Tafel slope, on the order of 40 mV/dec, was shown to be indicative for slow dioxygen (O-OH) bridge formation on the catalytic surface (cfr. reaction 5), combined with a high OH-coverage of the catalytic sites (θ_{MOH} > 0.8). This is also in agreement with the experimental findings of Lyons *et al.* on oxidised Fe electrodes.[50] Note that theoretically, an even lower Tafel slope around 30 mV/dec can be observed as well in two

particular cases : one for which reaction (4) is rate-determining (reconversion from hydroxyde to oxide) with still a high coverage of the empty state ($\theta_0 \cong 1$), and one for which reaction (6) is rate-determining, with a high coverage of MOH ($\theta_{MOH} > 0.6$). These cases however are not only rarely encountered in practice, but also not relevant for our own study, since the lowest Tafel slope values we observed are on the order of 41-46 mV/dec (cfr. Figure 7). In any case, the insights from ref. 49 and 50 applied to our own low Tafel slope regime directly confirms the relevance of attributing the observed upward shift of the (111) vs. (100) polarisation curve to a difference in hydroxide coverage. Indeed, for the underlying rds ($MO + OH^- \leftrightarrow MOOH + e^-$), it is indeed the hydroxyde coverage (θ_{MOH}) that determines the observed 40 mV/dec Tafel slope.

With respect to the higher values of the Tafel slope, a maximum Tafel slope value of 120 mV/dec has been calculated in ref. 49 for each of the above 5 reactions, provided the surface species formed in the step just before the rds is predominant. In our own case, we obtained at high over-potential even higher values, in the range 200-400 mV/dec. To the best of our knowledge, there is only other study so far that has reported such high Tafel slope values for the OER in alkaline media.[51] In that case, values as high as 292, 312 and 393 mV/dec were obtained in 1.0 M KOH on, respectively, $NiCo_2O_4$ nanoneedles, CoPi and $NiCo_2O_4$ nanosheets, without any further association to a specific chemical feature or rds. Nonetheless, by looking more carefully to the simulated graphs of ref. 49, it appears that in one specific case, slopes indeed tend to exceed the claimed theoretical maximum of 120 mV/dec. This is notably the case when reaction (6) becomes rate-determining ($MOOH + OH^- \leftrightarrow MOO^- + H_2O$) and at the same time the predominant surface species becomes the oxy-hydroxyde ($\theta_{MOOH} \rightarrow 1$). Moreover, it appears that the sooner (i.e. at lower current) θ_{MOOH} reaches full coverage, the closer the Tafel slope value will be to 120 mV/dec. As a result, this also confirms the relevance of our attributing the observed differences in Tafel slope between the (110) < (111) samples at high polarization to the underlying difference in the nature of the oxy-hydroxyde transformation, being more stable for 110 ($\beta \rightarrow \beta$) than for 111 ($\alpha \rightarrow \gamma$).

Conclusions

In conclusion, we have presented a number of experimental results showing that oriented NiO thin films have noticeable differences in their electrochemical properties towards the oxygen evolution reaction. The NiO 110 orientation has the highest electrochemical activity, which was attributed to the stabilization of the associated $Ni(OH)_2$ in its β form. On the contrary, both NiO 100 and NiO 111 are likely to produce on their surface the least active α-$Ni(OH)_2$ phase, whose coverage is smaller on the NiO 100 surface than on NiO 111.

Acknowledgements

We cordially thank Pierre Eloy and Joachim Brotz for carrying out the XPS and XRD measurements, respectively, and Alban Maton for machining the special tip for the rotating electrode. This work was funded by the European EJD-ITN project FunMAT (Project 641640).

References

1. Suen, N.-T.; Hung, S.-F.; Quan, Q.; Zhang, N.; Xu, Y.-J.; Chen, H. M. Electrocatalysis for the oxygen evolution reaction : recent development and future perspectives. *Chem. Soc. Rev.* **2017**, 46, 33-365.

2. Smith, R. D. L.; Prévot, M. S.; Fagan, R. D.; Zhang, Z.; Sedach, P. A.; Siu, M. K. J.; Trudel, S.; Berlinguette, C. P., Photochemical Route for Accessing Amorphous Metal Oxide Materials for Water Oxidation Catalysis. *Science* **2013,** *340*, 60-63.

3. Enman, L. J.; Burke, M. S.; Batchellor, A. S.; Boettcher, S. W., Effects of Intentionally Incorporated Metal Cations on the Oxygen Evolution Electrocatalytic Activity of Nickel (Oxy)hydroxide in Alkaline Media. *ACS Catalysis* **2016,** *6*, 2416-2423.

4. Klaus, S.; Louie, M. W.; Trotochaud, L.; Bell, A. T., Role of Catalyst Preparation on the Electrocatalytic Activity of Ni1–xFexOOH for the Oxygen Evolution Reaction. The Journal of Physical Chemistry C 2015, 119, 18303-18316.

5. Butera, V.; Toroker, M. C. Electronic Properties of Pure and Fe-Doped β-Ni(OH)2: New Insights Using Density Functional Theory with a Cluster Approach. *The Journal of Physical Chemistry C* **2016,** *120*, 12344-12350.

6. Hall, D. S.; Lockwood, D. J.; Bock, C.; MacDougall, B. R., Nickel hydroxides and related materials: a review of their structures, synthesis and properties. *Proc Math Phys Eng Sci* **2015,** *471*, 20140792.

7. Yeo, B. S.; Bell, A. T., In Situ Raman Study of Nickel Oxide and Gold-Supported Nickel Oxide Catalysts for the Electrochemical Evolution of Oxygen. *The Journal of Physical Chemistry C* **2012,** *116*, 8394-8400.

8. Doyle, R. L.; Lyons, M. E. G., The Oxygen Evolution Reaction: Mechanistic Concepts and Catalyst Design. In *Photoelectrochemical Solar Fuel Production*, 2016; pp 41-104.

9. Klaus, S.; Cai, Y.; Louie, M. W.; Trotochaud, L.; Bell, A. T., Effects of Fe Electrolyte Impurities on Ni(OH)2/NiOOH Structure and Oxygen Evolution Activity. *Journal of Physical Chemistry C* **2015,** *119*, 7243-7254.

10. Trotochaud, L.; Young, S. L.; Ranney, J. K.; Boettcher, S. W., Nickel-iron oxyhydroxide oxygen-evolution electrocatalysts: the role of intentional and incidental iron incorporation. *J Am Chem Soc* **2014,** *136*, 6744-53.

11. Görlin, M.; Chernev, P.; Ferreira de Araújo, J.; Reier, T.; Dresp, S.; Paul, B.; Krähnert, R.; Dau, H.; Strasser, P. Oxygen Evolution Reaction Dynamics, Faradaic Charge Efficiency, and the Active Metal Redox States of Ni−Fe Oxide Water Splitting Electrocatalysts. *J. Am. Chem. Soc.* **2016**, *138*, 5603–5614

12. Li, Y.-F.; Selloni, A., Mechanism and Activity of Water Oxidation on Selected Surfaces of Pure and Fe-Doped NiOx. *ACS Catalysis* **2014,** *4*, 1148-1153.

13. Sun, K.; Saadi, F. H.; Lichterman, M. F.; Hale, W. G.; Wang, H. P.; Zhou, X.; Plymale, N. T.; Omelchenko, S. T.; He, J. H.; Papadantonakis, K. M.; Brunschwig, B. S.; Lewis, N. S., Stable solar-driven oxidation of water by semiconducting photoanodes protected by transparent catalytic nickel oxide films. *Proc Natl Acad Sci U S A* **2015,** *112*, 3612-3617.

14. D'Amario, L.; Boschloo, G.; Hagfeldt, A.; Hammarström, L., Tuning of Conductivity and Density of States of NiO Mesoporous Films Used in p-Type DSSCs. *The Journal of Physical Chemistry C* **2014,** *118*, 19556-19564.

15. Brisse, R.; Faddoul, R.; Bourgeteau, T.; Tondelier, D.; Leroy, J.; Campidelli, S.; Berthelot, T.; Geffroy, B.; Jousselme, B., Inkjet Printing NiO-Based p-Type Dye-Sensitized Solar Cells. *ACS Appl Mater Interfaces* **2017,** *9*, 2369-2377.

16. Irwin, M. D.; Buchholz, D. B.; Hains, A.W.; Chang, R.P.H.; Marks, T.J. p-Type semiconducting nickel oxide as an efficiency-enhancing anode interfacial layer in polymer bulk-heterojunction solar cells. *PNAS* **2008**, *105*, 2783–2787.

17. Steirer, K. X.; Chesin, J. P.; Widjonarko, N. E.; Berry, J. J.; Miedaner, A.; Ginley, D. S.; Olson, D. C. Solution deposited NiO thin films as hole transport layers n organic photovoltaics. *Organic Electronics* **2010**, *11*, 1414-1418.

18. Liu, S.; Liu, R.; Chen, Y.; Ho, S.; Kim, J. H.; So F. Nickel Oxide Hole Injection/Transport Layers for Efficient Solution-Processed Organic Light-Emitting Diodes. *Chemistry of Materials* **2014**, *26*, 4528-4534.

19. Meher, S. K.; Justin, P.; Rao, G. R., Microwave-mediated synthesis for improved morphology and pseudocapacitance performance of nickel oxide. *ACS Appl Mater Interfaces* **2011,** *3*, 2063-73.

20. Hu, G.; Li, C.; Gong, H., Capacitance decay of nanoporous nickel hydroxide. *Journal of Power Sources* **2010,** *195*, 6977-6981.

21. Islam, R. ; Ramesh, P.; Nam, J. Y.; Saraswat, K.C. (2015). Nickel oxide carrier selective contacts for silicon solar cells. IEEE 42nd Photovoltaic Specialists Conference (PVSC) **2015**, 1-4.

22. Miller, E. L.; Rocheleau, R. E., Electrochemical and Electrochromic Behavior of Reactively Sputtered Nickel Oxide. *Journal of the Electrochemical Society* **1997,** *144*, 9.

23. Nadesan, J. C. B.; Tseung, A. C. C., Oxygen Evolution on Nickel-Oxide Electrodes. *Journal of the Electrochemical Society* **1985,** *132*, 2957-2959.

24. Kelsey A. Stoerzinger, L. Q., Orientation-Dependent Oxygen Evolution Activities of Rutile IrO2 and RuO2. Physical Chemistry Letter 2014, 1636−1641.

25. Goniakowski, J.; Finocchi, F.; Noguera, C., Polarity of oxide surfaces and nanostructures. *Reports on Progress in Physics* **2008,** *71* (1).

26. Tasker, P. W.; Duffy, D. M.; The structure and properties of the stepped surfaces of MgO and NiO. *Surface Science Letters* **1984**, *137*, 91-102.

27. Warota, B.; Snoecka, E.; Baulès, P.; Ousseta, J. C.; Casanovea, M. J.; Dubourgb, S.; Bobob, J. F., Original surface morphology of epitaxial NiO layers grown on MgO(1 1 0). *Journal of Crystal Growth* **2001,** (224), 7.

28. Warot, B.; Snoeck, E.; Ousset, J. C.; Casanove, M. J.; Dubourg, S.; Bobo, J. F., Surface morphology of NiO layers on MgO(0 0 1), MgO(1 1 0) and MgO(1 1 1). *Applied Surface Science* **2002,** *188*, 151-155.

29. Warot, B.; Snoeck, E.; Baulès, P.; Ousset, J. C.; Casanove, M. J.; Dubourg, S.; Bobo, J. F., Epitaxial growth of NiO layers on MgO(0 0 1) and MgO(1 1 0). *Applied Surface Science* **2001,** *177* (4), 287-291.

30. Warota, B.; Snoecka, E.; Baules, P.; Ousseta, J. C.; Casanovea, M. J.; Dubourgb, S.; Bobob, J. F., Formation of tetrahedral islands in epitaxial NiO layers deposited on MgO(1 1 1). *Journal of Crystal Growth* **2002,** (234), 7.

31. Barbier, A.; Mocuta, C.; Kuhlenbeck, H.; Peters, K. F.; Richter, B.; Renaud, G., Atomic Structure of the Polar NiO(111)-p(2x2) Surface. *Physical review Letters* **2000,** *84*, 3.

32. Zhao, W.; Bajdich, M.; Carey, S.; Vojvodic, A.; Nørskov, J. K.; Campbell, C. T., Water Dissociative Adsorption on NiO(111): Energetics and Structure of the Hydroxylated Surface. *ACS Catalysis* **2016,** *6*, 7377-7384.

33. Zhang, W. B.; Tang, B. Y., Stability of the polar NiO(111) surface. *J Chem Phys* **2008,** *128*, 124703.

34. Langell, M. A.; Nassir, M. H., Stabilization of NiO(111) Thin Films by Surface Hydroxyls. *Journal of Physical Chemistry* **1995,** *99*, 7.

35. Kitakatsu, N.; Maurice, V.; Hinnen, C.; Marcus, P. Surface hydroxylation and local structure of NiO thin films formed on Ni(111). *Surface Science* **1998***, 407,* 36-58.

36. Mohsenzadeh, A.; Bolton, K.; Richards, T.E. DFT study of the adsorption and dissociation of water on Ni(111), Ni(110) and Ni(100) surfaces. *Surface Science* **2014**, *627*, 1-10.

37. Tench, D.; Ogden, C. The Effect of Depassivation at Specific Crystal Facets on the State of Activation of Nickel Substrates for Electrodeposition. *Journal of the Electrochemical Society* **1978**, *125*, 1940-1945.

38. Jang, W. L.; Lu, Y. M.; Hwang, W. S.; Hsiung, T. L.; Wang, H. P., Effect of substrate temperature on the electrically conductive stability of sputtered NiO films. *Surface & Coatings Technology* **2008,** *202*, 5444-5447.

39. Ryu, H.-W.; Choi, G.-P.; Hong, G.-J.; Park, J.-S., Growth and Surface Morphology of Textured NiO Thin Films Deposited by Off-Axis RF Magnetron Sputtering. *Japanese Journal of Applied Physics* **2004,** *43*, 5524-5525.

40. Hirschorn, B.; Orazem, M. E.; Tribollet, B.; Vivier, V.; Frateur, I.; Musiani, M., Determination of effective capacitance and film thickness from constant-phase-element parameters. *Electrochimica Acta* **2010,** *55*, 6218-6227.

41. Lindahl, E.; Lu, J.; Ottosson, M.; Carlsson, J. O., Epitaxial NiO (100) and NiO (111) films grown by atomic layer deposition. *Journal of Crystal Growth* **2009,** *311*, 4082-4088.

42. Lee, J. H.; Kwon, Y. H.; Kong, B. H.; Lee, J. Y.; Cho, H. K., Biepitaxial Growth of High-Quality Semiconducting NiO Thin Films on (0001) Al_2O_3 Substrates: Microstructural Characterization and Electrical Properties. *Crystal Growth & Design* 2012, 12 (5), 2495-2500.

43. McIntyre, N. S.; Zetaruk, D. G., X-Ray Photoelectron Spectroscopic Studies of Iron-Oxides. Analytical Chemistry 1977, 49 (11), 1521-1529.

44. Su, D.; Ford, M.; Wang, G., Mesoporous NiO crystals with dominantly exposed {110} reactive facets for ultrafast lithium storage. *Sci Rep* **2012,** *2*, 924.45. Hu, G.; Li, C.; Gong, H., Capacitance decay of nanoporous nickel hydroxide. *Journal of Power Sources* **2010,** *195* (19), 6977-6981.

46. Morrison, S. R., *Electrochemistry at Semiconductor and Oxidized Metal Electrodes*. Second Edition (1984) ed.; Plenum Press: New York, 1980.

47. Cappus, D.; Xu, C.; Ehrlich, D.; Dillmann, B.; Ventrice, C. A.; Alshamery, K.; Kuhlenbeck, H.; Freund, H. J., Hydroxyl-Groups on Oxide Surfaces - Nio(100), Nio(111) and Cr2o3(111). *Chemical Physics* **1993,** *177*, 533-546.

48. Schulze, M.; Reissner, R.; Lorenz, M.; Radke, U.; Schnurnberger, W., Photoelectron study of electrochemically oxidized nickel and water adsorption on defined NiO surface layers. *Electrochimica Acta* **1999,** *44*, 8.

49. Shinagawa, T.; Garcia-Esparza, A. T.; Takanabe, K., Insight on Tafel slopes from a microkinetic analysis of aqueous electrocatalysis for energy conversion. *Sci Rep* **2015,** *5*, 13801.

50. Lyons, M. E. G.; Doyle, R. L., Oxygen Evolution at Oxidised Iron Electrodes: A Tale of Two Slopes. *International Journal of Electrochemical Science* **2012**, 7, 14.

51. Shi H., Zhao G, Water Oxidation on Spinel NiCo2O4 Nanoneedles Anode: Microstructures, Specific Surface Character, and the Enhanced Electrocatalytic Performance, *J. Phys. Chem. C* **2014**, *118*, 25939−25946

Figure legends

Figure 1. Bode representation of the Ni hydroxide/oxy-hydroxide phase transformation cycle

Figure 2. Typical electrochemical protocol. Cyclic Voltammetry (CV) and Electrochemical Impedance Spectroscopy (EIS) are not represented by boxes. Raw data is taken from electrochemical measurement on NiO 111. On this graph, it can also be seen that current during the chrono-amperometry is stable and relatively close to the value obtained during the quasi-static experiment.

Figure 3. X-ray diffractograms for our NiO 111, 100 and 110 samples before (top) and after (bottom) electrochemical experiments. NiO peaks are indicated by their orientation, * and **represent peaks from the MgO and Pt substrates, respectively.

Figure 4. AFM phase pictures before electrochemical cycling of (a) NiO 100, (b) NiO 110, (c) NiO 111

Figure 5. From top to bottom : XPS profiles after electrochemical cycling of, respectively, Ni2p(3/2), O1s and Fe2p regions for NiO 100, NiO 111 and NiO 110.

Figure 6. I-V curves, both in linear (left) and semi-logarithmic scale (right). The potential is iR corrected. Data from cyclic voltammetry at slow scan rate (10 mV/s) are superposed on the quasi-static (QS) points.

Figure 7. Tafel slopes at low and high overpotential on the different orientations. Errors bars represent the standard deviation on the semi-logarithmic fit of the Tafel slope in Fig. 6.

Figure 8. Cyclic voltammograms at 100 mV/s in the $Ni(OH)_2$ pre-oxidation wave region. Black dots represent boundaries for determining columbic charge of the oxidation and reduction wave.

Figure 9. EIS realized at 1.45 vs RHE on the different sample and represented in Nyquist plot.

Figure 10. Helmholtz layer values (top) and charge transfer resistances (bottom) for the NiO 100, 110 and 111 orientations, as determined by EIS at different potentials. The error bars have been

calculated based on the relevant formulas for statistical error propagation based on original eq. (1) and the fitting errors directly provided by the EIS software on α, Q, R_{el} and R_{cpe}.

Tables and figures

Table 1 : Surface properties of NiO 100, 110 and 111 orientations: a) structural representation of surface termination, b) inter-plane distances and c) surface energies.[26]

	NiO 100 – non polar	NiO 110 – non polar	NiO 111 - polar
a)	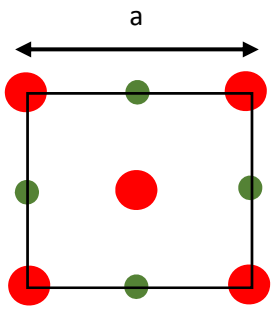	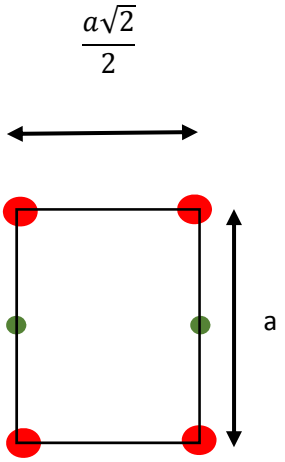	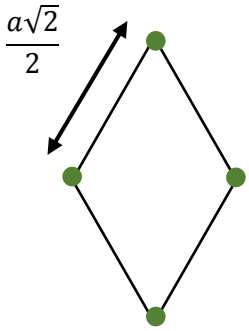
b)	4.17 Å	2.95 Å	2.41 Å
c)	1.15 J/m²	2.77 J/m²	Infinity (if not reconstructed)

Table 2: Deposition parameters

Power	40 W
Pressure	0,5 Pa
Temperature	500°C
Target-to-substrate distance	14 cm

Table 3: Value of the resistance *E(vs. Ag/AgCl)$^{-0.864}$, for correcting I-V curves according to the surface orientation. The resistance values were estimated from EIS.

NiO 100	NiO 110	NiO 111
16.3	14.0	11.5

Table 4 : Main results from AFM measurements.

	RMS height (nm)	Geometrical surface ratio	Average grain size (nm)
NiO 100	3.0	1.021	52 ± 2
NiO 111	10.5	1.066	78 ± 2
NiO 110	6.7	1.024	105 ± 2

Table 5: Area fraction extrapolated from XPS deconvolution on the different orientations.

	NiO 100	NiO 111	NiO 110
theoretical Ni atomic surface density (at/Å^2)	0.115	0.133	0.081
O-Ni (%)	22.5	15.8	11.7
OH-Ni (%)	54.0	54.7	60.0
O-C (%)	23.5	29.5	28.3
Ratio OH-Ni/O-Ni	2.4	3.5	5.1
Estimated hydroxide thickness (nm)	1.4	1.7	2.1
Estimated carbonated layer (nm)	1.5	1.9	1.9

Table 6: Main characteristics of the oxidation and reduction wave of the hydroxide/oxy-hydroxide reaction before OER. Raw data taken from cyclic voltammetry realized at 100 mV/s.

	FW peak (V vs RHE)	BW peak (V vs RHE)	FW peak (µC/cm²)	BW peak (µC/cm²)	C (µF/cm²) @ 1.45 V vs. RHE
NiO 100	1,36	1,26	231	-202 (87%)	590
NiO 111	1,37	1,28	808	-692 (85%)	905
NiO 110	1,37	1,30	538	-632 (115%)	965

Table 7: EIS equivalent electric circuit model according to the NiO orientation. Electric circuit for the NiO 100 was adapted from Morrison.[46]

NiO 111 & NiO 110	NiO 100
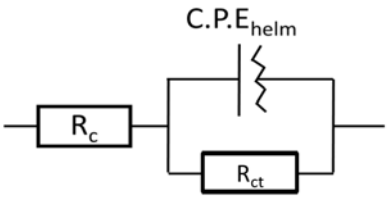	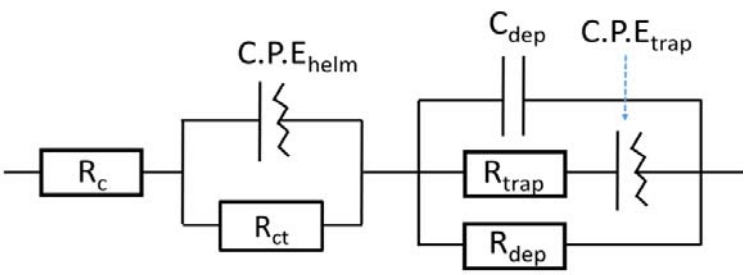

Table 8 : Extracted parameter values from fitting the EIS spectra to the equivalent circuit shown in Table 7. R_c represents the contact resistance, R_{ct} accounts for the charge transfer resistance, and C_{eq} is the equivalent capacitance of the Helmholtz double layer. The electrode area was 0.2 cm^2 in all cases.

NiO 110					
Potential vs RHE (V)	Current (mA/cm^2)	R_c (Ohm)	R_{ct} (Ohm)	N	C_{eq} ($\mu F/cm^2$)
1.45	0.13	16.5	814	0.91	658.2
1.55	5.46	15.8	23.9	0.92	522.6
1.65	19.49	12.5	6.8	0.92	376.3
1.75	37.92	12.3	4.2	0.92	296.6

NiO 111					
Potential vs RHE (V)	Current (mA/cm^2)	R_c (Ohm)	R_{ct} (Ohm)	N	C_{eq} ($\mu F/cm^2$)
1.45	0.35	28.3	482	0.92	713.9
1.55	7.10	11.4	9.41	0.92	541.0
1.65	18.95	11.6	3.73	0.94	423.9
1.75	31.07	11.6	2.61	0.89	405.2

NiO 100									
Potential vs RHE (V)	Current (mA/cm^2)	R_c (Ohm)	R_{ss} (Ohm)	N_{ss}	R_{sc} (Ohm)	C_{sc} (nF)	R_{ct} (Ohm)	N	C_{eq} ($\mu F/cm^2$)
1.45	0.04	9.59	37.2	0.65	21.9	17.7	1370	0.86	328.9
1.55	2.67	9.59	31.8	0.60	16.9	16.6	27.7	0.89	262.0
1.65	8.64	9.59	42.2	0.73	13	16.2	9.56	0.88	175.8
1.75	15.27	9.59	58.4	0.97	11.9	11	5.74	0.85	137.6

Table 9 : Number of exchanged electrons per cationic site during the pre-OER hydroxide/oxy hydroxide forward (FW) oxidation wave, based on the values for the theoretical Ni-atomic density and the number of electrons per unit surface determined from the specific charge values for the FW wave in Table 6. Dividing these values by the relevant cationic density of $Ni(OH)_2$ then provides an "electrochemical" estimation of the Ni hydroxyde thicknesses.

	NiO 100	**NiO 110**	**NiO 111**
Ni-cations /Å^2 (theoretical)	0.115	0.081	0.133
electrons / Å^2 (FW oxidation wave)	0.144	0.336	0.505
electrons/Ni-cation (FW oxidation wave)	1.25	4.15	3.80
electrochemical thickness (nm, from FW wave) β) 1 e^-/Ni (β→β phase) γ) 1.67 e^-/Ni (α→γ phase)	β) 0.55 γ) 0.33	β) 1.29 γ) 0.77	β) 1.94 γ) 1.16

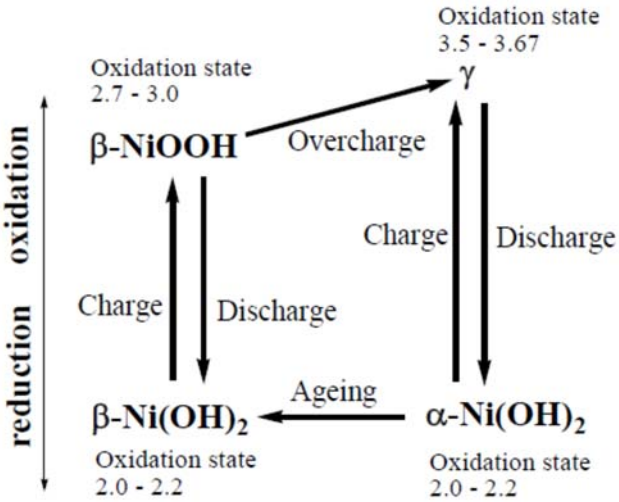
Oxidation state
3.5 - 3.67
γ
Oxidation state
2.7 - 3.0
β-NiOOH
Overcharge
oxidation
reduction
Charge
Discharge
Charge
Discharge
Ageing
β-Ni(OH)2
α-Ni(OH)2
Oxidation state
2.0 - 2.2
Oxidation state
2.0 - 2.2

Figure 1

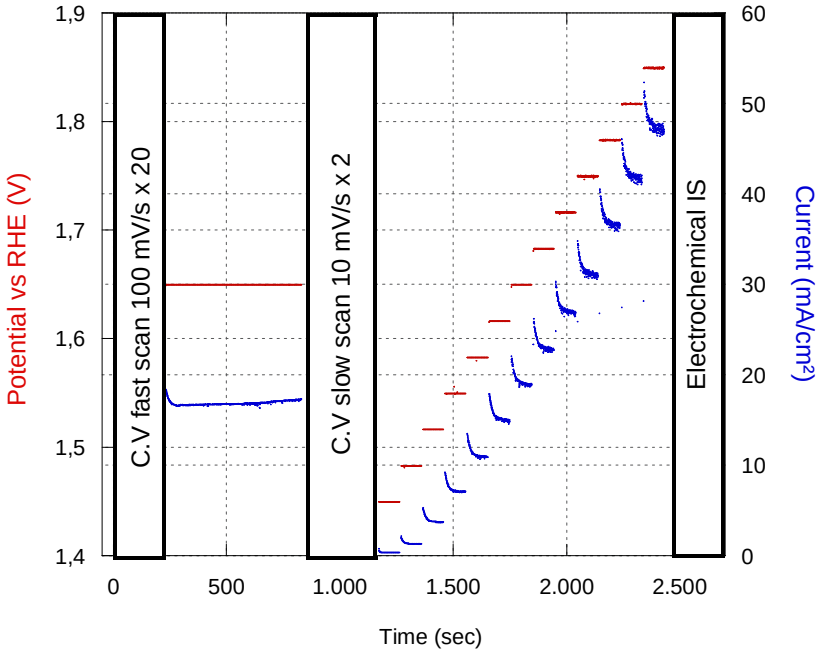
1,9
1,8
1,7
1,6
1,5
1,4
Potential vs RHE (V)
60
50
40
30
20
10
0
Current (mA/cm²)
C.V fast scan 100 mV/s x 20
C.V slow scan 10 mV/s x 2
Electrochemical IS
0
500
1.000
1.500
2.000
2.500
Time (sec)

Figure 2

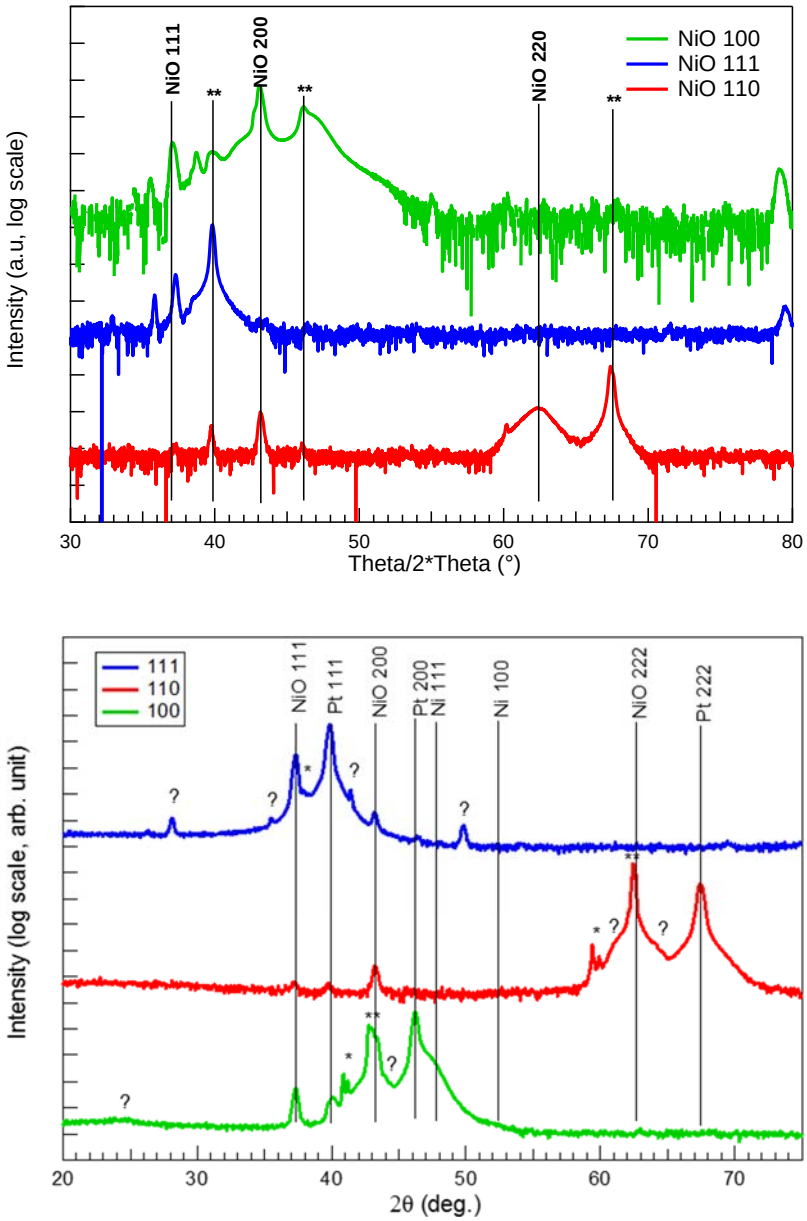
NiO 111
NiO 200
NiO 220
NiO 100
NiO 111
NiO 110
Intensity (a.u, log scale)
Theta/2*Theta (°)
111
110
100
NiO 111
Pt 111
NiO 200
Pt 200
Ni 111
Ni 100
NiO 222
Pt 222
Intensity (log scale, arb. unit)
2θ (deg.)

Figure 3

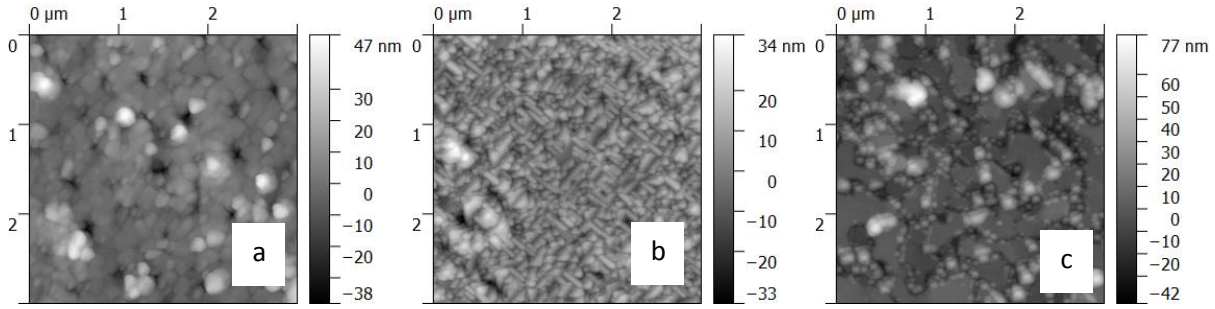
0 µm
1
2
0
1
2
47 nm
30
20
10
0
−10
−20
−38
a
0 µm
1
2
0
1
2
34 nm
20
10
0
−10
−20
−33
b
0 µm
1
2
0
1
2
77 nm
60
50
40
30
20
10
0
−10
−20
−42
c

Figure 4

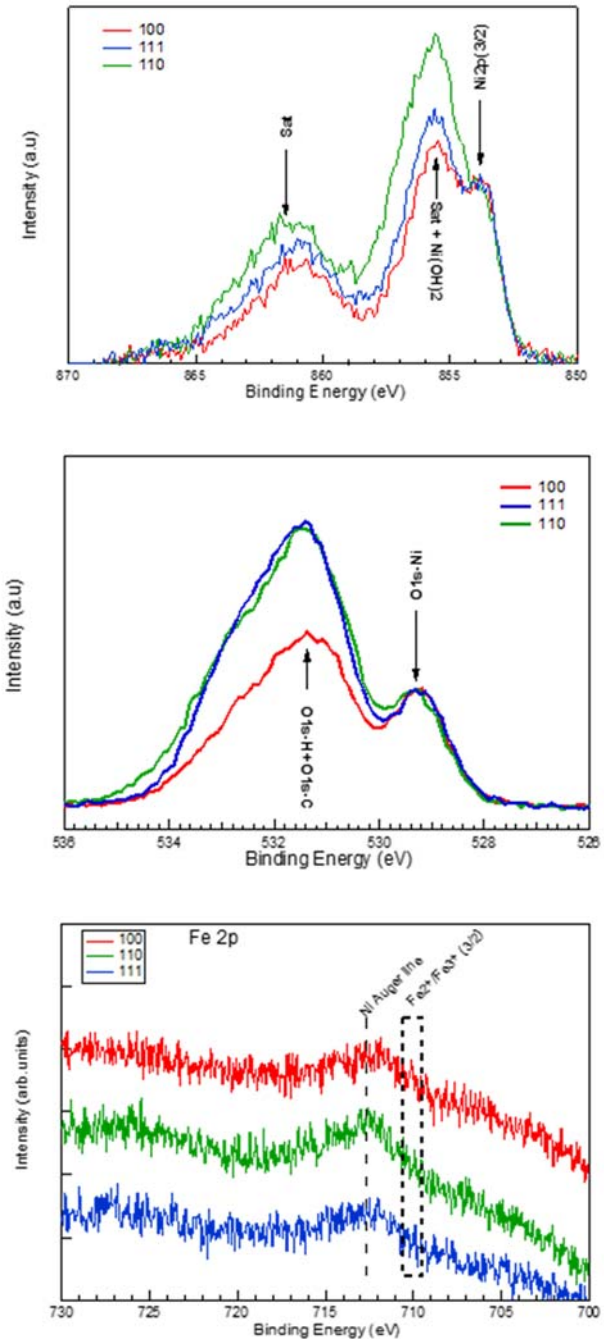
100
111
110
Sat
Sat + Ni(OH)2
Ni2p(3/2)
Intensity (a.u)
870
865
860
855
850
Binding Energy (eV)
100
111
110
O1s-Ni
O1s-H+O1s-C
Intensity (a.u)
536
534
532
530
528
526
Binding Energy (eV)
Fe 2p
100
110
111
Ni Auger line
Fe2+Fe3+ (3/2)
Intensity (arb. units)
730
725
720
715
710
705
700
Binding Energy (eV)

Figure 5

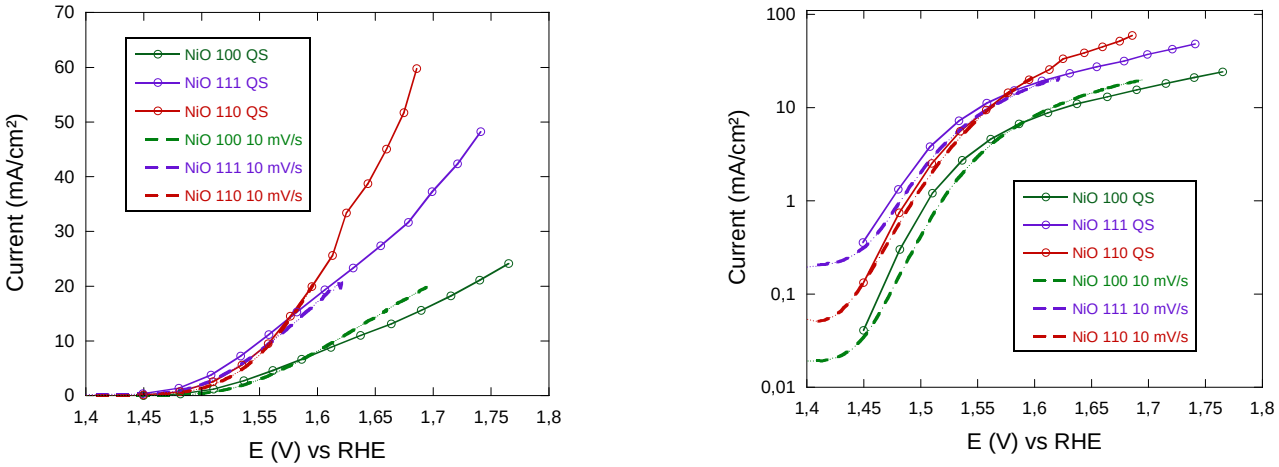
Current (mA/cm²)
E (V) vs RHE
NiO 100 QS
NiO 111 QS
NiO 110 QS
NiO 100 10 mV/s
NiO 111 10 mV/s
NiO 110 10 mV/s
70
60
50
40
30
20
10
0
1,4
1,45
1,5
1,55
1,6
1,65
1,7
1,75
1,8
100
10
1
0,1
0,01

Figure 6

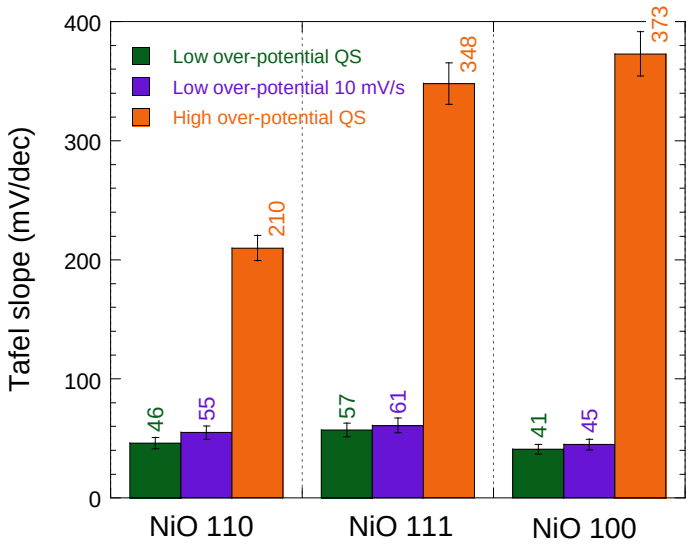
Tafel slope (mV/dec)
400
300
200
100
0
Low over-potential QS
Low over-potential 10 mV/s
High over-potential QS
46
55
210
57
61
348
41
45
373
NiO 110
NiO 111
NiO 100

Figure 7

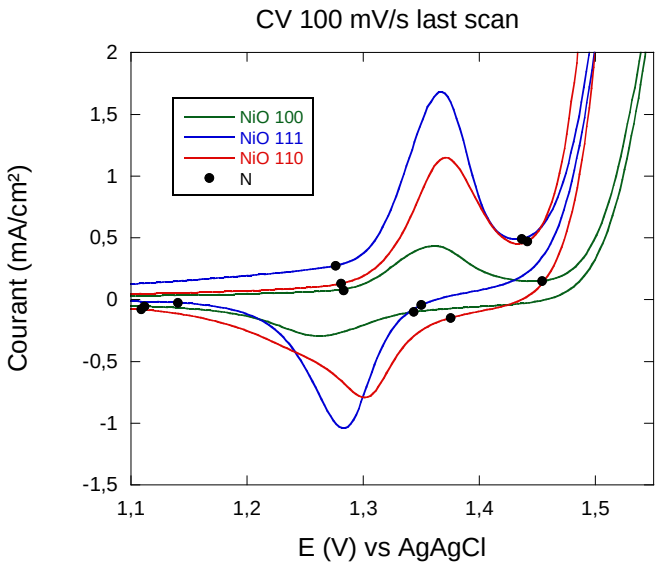
CV 100 mV/s last scan
Courant (mA/cm²)
E (V) vs AgAgCl
NiO 100
NiO 111
NiO 110
N
2
1,5
1
0,5
0
-0,5
-1
-1,5
1,1
1,2
1,3
1,4
1,5

Figure 8

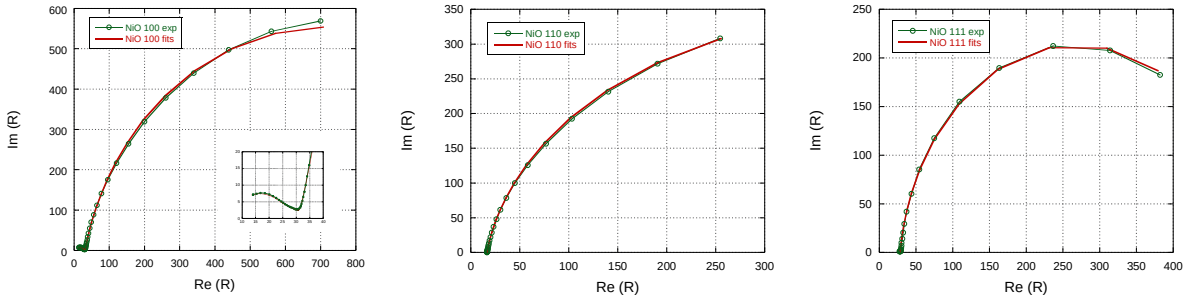
NiO 100 exp
NiO 100 fits
Im (R)
Re (R)
NiO 110 exp
NiO 110 fits
Im (R)
Re (R)
NiO 111 exp
NiO 111 fits
Im (R)
Re (R)

Figure 9

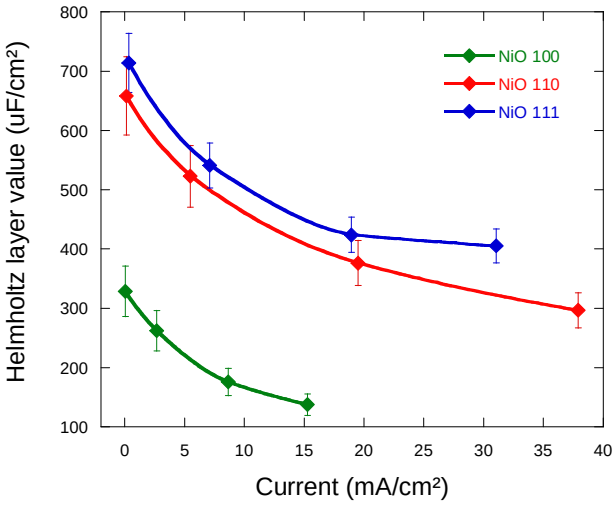
Helmholtz layer value (uF/cm²)
Current (mA/cm²)
NiO 100
NiO 110
NiO 111
800
700
600
500
400
300
200
100
0
5
10
15
20
25
30
35
40

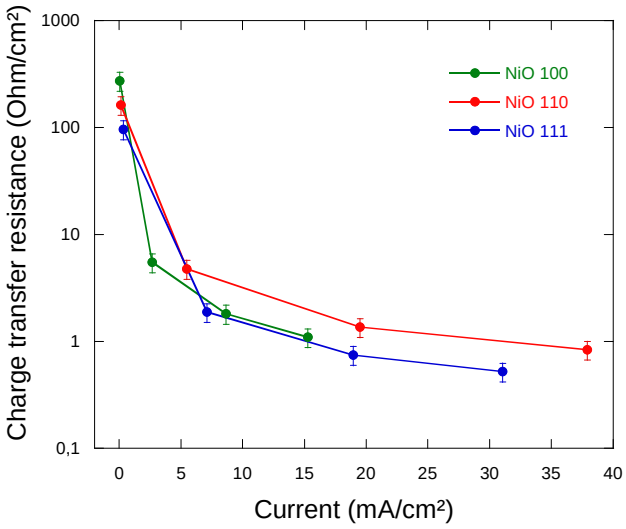
Charge transfer resistance (Ohm/cm²)
Current (mA/cm²)
NiO 100
NiO 110
NiO 111
1000
100
10
1
0,1
0
5
10
15
20
25
30
35
40

Figure 10